# Factors in the Metal Doping of BiVO4 for Improved Photoelectrocatalytic Activity as Studied by Scanning Electrochemical Microscopy and First-Principles Density-Functional Calculation

Hyun S. Park,[†] Kyoung Eun Kweon,[‡] Heechang Ye,[†] Eunsu Paek,[§] Gyeong S. Hwang,[§] and Allen J. Bard*,[†]

[†]Center for Electrochemistry, Department of Chemistry and Biochemistry, [‡]Department of Electrical and Computer Engineering, and [§]Department of Chemical Engineering, The University of Texas at Austin, Austin, Texas 78712, United States

Ⓢ *Supporting Information*

ABSTRACT: Metal doping of the metal oxide photoelectrocatalyst, BiVO4, dramatically increases its activity for water oxidation. Scanning electrochemical microscopy (SECM) was used to screen various dopants for their photoelectrochemical performance and to optimize the used dopant material concentrations with this photocatalyst. For example, adding Mo to W-doped BiVO4 enhanced the performance. The photocatalytic activity was examined on larger electrodes by means of photoelectrochemical and electrochemical measurements. The developed photoelectrocatalyst, W- and Mo-doped BiVO4, shows a photocurrent for water oxidation that is more than 10 times higher than undoped BiVO4. Factors that affect performance are discussed, and enhanced separation of excited electron—hole pairs by doping onto the semiconductor is suggested by first-principles density-functional theory (DFT) calculations. Distortion of the crystal structure of monoclinic scheelite-like BiVO4 by addition of W and Mo doping predicted by DFT is also revealed by X-ray diffraction and Rietveld refinement analysis. The results indicate that the consecutive doping of W and Mo into the metal oxide photocatalyst introduces improved electron—hole separation without a significant change of the band gap or the material's optical properties.
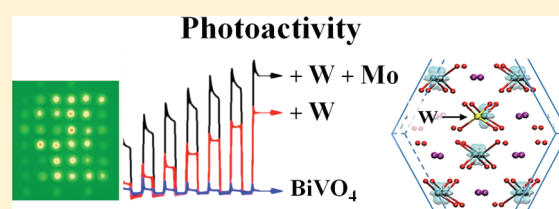
■ INTRODUCTION

The semiconductor properties important in the design of photocatalysts required for a photosynthetic system, e.g., a photoelectrochemical cell to split water to hydrogen and oxygen, have largely been taken to be the band gap energy, E_g, and the band-edge locations, E_c and E_v (usually with considerations of factors affecting stability).[1,2] These affect the amount of solar energy absorbed in the material and the energies of electrogenerated carriers (holes and electrons). However, many other factors affect the performance and efficiency of the photocatalyst, such as the depth of penetration of the incident radiation, the carrier mobility, the depth of the electric field at the surface, the rate of recombination of the photogenerated carriers in the bulk and on the surface, and the carrier transfer rate to solution species. Clearly, both the photocatalyst composition and its structure are important.

Combinatorial screening of the photocatalysts has been used to find new photocatalysts including scanning electrochemical microscopy (SECM) based on scanning with a fiber optic and robotic fabrication of arrays; these have been useful in finding photocatalysts with the desired composition.[3−10] The rapid screening by SECM of metal oxide and metal sulfide semiconductors has been useful in finding highly active photocatalysts. For example, we recently developed W-doped BiVO4, which has several times higher photoactivity for water oxidation than undoped BiVO4.[9] Solid solutions of $Zn_xCd_{1−x}Se_yS_{1−y}$ were also

developed using the SECM screening method to find the optimum values of x and y to tune the band gap and photoelectrochemical activity for polysulfide oxidation.[10] Development of an excellent photocatalyst with high conversion efficiency for light, along with electrocatalysts to drive the desired reactions, is essential in the design of the overall photoelectrochemical system to achieve the photosynthetic production of a fuel, such as hydrogen from water. SECM as described above has been proven to be a very useful tool for discovering a complicated composition with optimal properties.

In the nearly 40 years since Fujishima and Honda suggested the possibility of water splitting in a photoelectrochemical cell,[11] there have been enormous efforts to find a photocatalyst and electrocatalysts for this reaction. However, to date none of these investigated photocatalysts has fulfilled all of the necessary design requirements for practical photosynthetic water splitting.[12] BiVO4 is a promising material that can adopt a wide range of dopants with doping levels of 10 atomic percent (at %) or more to tune its optical and chemical properties.[13,14] BiVO4 has a band gap of 2.4—2.5 eV which harvests visible light, and it has been studied as a water oxidation photocatalyst.[15−21] Furthermore, the photocatalytic activity of BiVO4 also depends on its crystal

structure, and the monoclinic scheelite-like $BiVO_4$ is a much more active structure than a tetragonal scheelite or tetragonal zircon structure.[15] To improve the photoactivity, chemical treatment of $BiVO_4$ has also been investigated. Soaking of $BiVO_4$ films in aqueous $AgNO_3$ solution is suggested as a material treatment to enhance its stability and photocatalytic activity for water oxidation.[16] As mentioned above, doping of a fourth material into the $BiVO_4$ has also been studied to increase the photoactivity, and W is an excellent dopant for $BiVO_4$ using the SECM screening method.[9] However, the relationship between the material properties or chemical treatments described above and the photocatalytic activity has not been explained, and few studies are reported based on first-principles calculations.[13,17]

Herein, we demonstrate a further increase in the photoelectrocatalytic activity of W-doped $BiVO_4$ by additional doping with Mo. A robotic dispensing system was used to prepare a photocatalyst array with different dopants based on W-doped $BiVO_4$. These arrays were screened by SECM. First-principles density-functional theory (DFT) calculations were carried out and suggest a possible explanation of the enhanced photoelectrochemical activity of the $Bi-V-W-Mo-O$ material.

■ EXPERIMENTAL SECTION

Chemicals. $Bi(NO_3)_3 \cdot 5H_2O$ (99.999%) and $(NH_4)_{10}H_2\text{-}(W_2O_7)_6 \cdot xH_2O$ (99.99%) were obtained from Strem Chemicals (Newburyport, MA). Na_2HPO_4 (99.9%), NaH_2PO_4 (99.5%), and ethylene glycol were purchased from Fisher Scientific (Pittsburgh, PA). VCl_3 (99%, Alfa-Aeser, Ward Hill, MA), $(NH_4)_6\text{-}Mo_7O_{24} \cdot 4H_2O$ (99.98%, Sigma-Aldrich, St. Louis, MO), Na_2SO_4 (99.0%, Sigma-Aldrich, St. Louis, MO), and Na_2SO_3 (99.6%, Mallinckrodt Baker, Phillipsburg, NJ) were used as received. Fluorine-doped tin oxide (FTO, TEC 15, Pilkington, Toledo, OH) was used as a substrate for dispensed arrays of metal oxide and as a substrate for the bulk film electrode. Deionized Milli-Q water was used as the solvent in electrochemical experiments.

Electrodes. Photocatalyst arrays were fabricated using a CH Instruments model 1550 dispenser (Austin, TX) consisting of a stepper-motor based XYZ positioner with a piezoelectric dispensing tip. The dispensing system was connected to a personal computer to control the position of the piezoelectric jetting tip. The tip is robotically moved to a programmed position over the conducting substrate, and jetting is performed from the tip by applying a potential of 80 V for 40 μs. The distance between two photocatalyst spots on the array was about 800 μm with a spot diameter of about 500 μm. Each spot had a total of 18 drops of the precursor solutions of $Bi-V$ (5:5 in atomic ratio, total concentration of 0.1 or 0.02 M), W (0.02 M), and the fifth material (0.02 M). The relative number of dispensed drops from each solution was controlled to obtain the targeted spot composition. After completing the dispensing, the arrays were annealed in air at 500 °C for 3 h and ramped from room temperature to 500 °C at a ramp rate of 1 °C per minute.

The bulk metal oxide semiconductor thin film electrodes were prepared on FTO by drop casting using 100 μL of precursor solution with total concentrations of 5 mM and the targeted atomic compositions. The bulk film was also annealed in air at 500 °C for 3 h.

Instruments. A CH Instruments model 990B SECM potentiostat (Austin, TX) was used to control the fiber optic position and collect the photocurrent from dispensed arrays on FTO. A CH Instruments model 630D Electrochemical Analyzer was used

as a potentiostat for the experiments with thin film electrodes. A platinum gauze counter electrode and a Ag/AgCl reference electrode in 3 M KCl solution were used to complete the three electrode configuration. However, the potential reported here is quoted with respect to the normal hydrogen electrode (NHE). Conductance measurements were performed using a model 1286 electrochemical interface and model 1250 frequency response analyzer (Solatron Analytical, Hampshire, England). Electrochemical impedance spectroscopy was conducted in 0.1 M Na_2SO_4 solution with an AC amplitude of 10 mV at each applied potential, and measurements were conducted at three different frequencies: 200, 500, and 1000 Hz. For photoelectrochemical measurements, illumination was with a Xenon lamp (XBO 150 W, Osram, Munich, Germany) with full output for UV–visible irradiation or with a 420 nm cutoff filter (WBF-3, Oriel, Darmstadt, Germany) for visible irradiation. A monochromator (Photon Technology International, Birmingham, NJ), silicon photodetector (model 818-UV, Newport, Irvine, CA), and optical power meter (model 1830-C, Newport, Irvine, CA) were used to obtain the incident photon to current conversion efficiency (IPCE).

UV–visible absorption spectra were acquired with a Milton Roy Spectronic 3000 array spectrophotometer (New Rochelle, NY) for wavelengths from 320 to 900 nm. X-ray diffraction (XRD) measurements were performed using a Bruker-Nonius D8 advanced powder diffractometer (Madison, WI) operated at 40 kV and 40 mA with Cu Kα radiation (λ = 1.54 Å). Grazing incidence XRD (GIXRD) with an incidence angle of 1° on detector scan mode was performed to obtain the diffractogram from the thin film electrodes on FTO. The scan rate was 12° per minute in 0.02° increments of 2θ from 10° to 90°. The obtained diffractogram was analyzed using the Material Analysis Using Diffraction (MAUD) program developed by Luca Lutterotti.[22] MAUD analysis is based on the Rietveld refinement method. Fitting of XRD patterns using MAUD was continued until refinement reliability factors, such as R_w and σ, become less than 10 and 2.

■ COMPUTATIONAL METHODS

The calculations reported herein were performed on the basis of spin-polarized density functional theory (DFT) within the Perdew–Burke–Ernzerhof (PBE) generalized gradient approximation (GGA),[23] as implemented in the Vienna ab initio Simulation Package (VASP).[24] The projector augmented wave (PAW) method with a plane wave basis set was used to describe the interaction between ion cores and valence electrons.[25] The valence electron configurations considered are: $5d^{10}6s^26p^3$ for Bi; $3p^63d^34s^2$ for V; $2s^22p^4$ for O; and $3p^63d^54s^1$ ($4p^64d^55s^1$, $5p^65d^46s^2$) for Cr (Mo, W). The monoclinic $BiVO_4$ structure was determined through careful volume optimization and atomic position relaxation with a primitive unit cell (consisting of two $BiVO_4$ units); here, energy cutoffs of 750 eV (volume optimization) and 650 eV (atomic relaxation) were applied for the plane wave expansion of the electronic eigenfunctions, and a gamma-centered (6 × 6 × 6) Monkhorst–Pack mesh[26] of k points was used for the Brillouin zone sampling. The calculated lattice parameters are a = 7.285 Å, b = 11.763 Å, c = 5.123 Å, and β = 134.18°, close to the experimental values[27] of a = 7.247 Å, b = 11.702 Å, c = 5.096 Å, and β =134.18°. For doped $BiVO_4$ systems, we used a 2 × 2 × 2 supercell (comprised of 16 $BiVO_4$ units); a plane wave cutoff
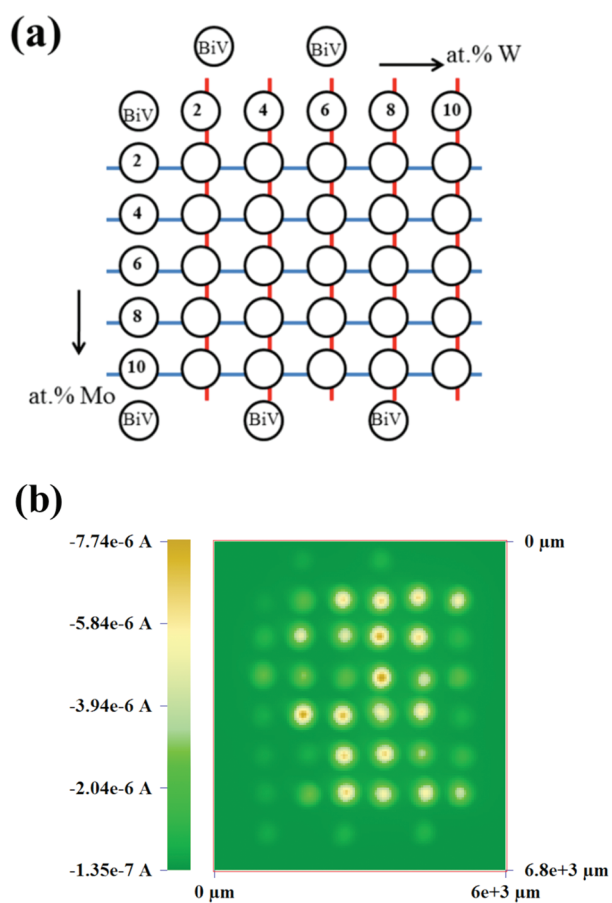
Figure 1. (a) Schematic diagram of the atomic composition of dispensed photoelectrocatalysts on FTO. Each spot has a total of 18 drops of the precursor solutions of Bi/V (0.1 or 0.02 M), W (0.02 M), and Mo (0.02 M) in ethylene glycol. (b) SECM image of Bi/V/W/Mo oxide photoelectrocatalysts dispensed on FTO with different doping levels of W and Mo as shown in (a). The photocurrent for sulfite oxidation was measured at 0.4 V vs NHE in 0.1 M Na_2SO_3 and 0.1 M Na_2SO_4 solution under UV—visible irradiation. The scan rate of fiber optic was 500 μm s^{-1} (or 50 μm per 0.1 s as the setting condition of SECM), and the distance between the fiber optic and substrate was 150 μm.

energy of 500 eV and a gamma-centered $(2 \times 2 \times 2)$ k-point mesh were used to calculate geometries and total energies during geometry optimization, while the k-point mesh size was increased up to $(4 \times 4 \times 4)$ to reevaluate corresponding electronic structures. In the geometry optimization, all atoms were fully relaxed using a conjugate gradient method until residual forces on constituent atoms became smaller than 3×10^{-2} eV/ Å. For selected systems, we also used DFT (GGA)+U within Dudarev's approach.[28]

■ EXPERIMENTAL RESULTS AND DISCUSSION

Preparation and SECM Scanning of Bi—V—W—O—M Arrays. Photoelectrocatalyst arrays based on $BiVO_4$ with different levels of W and Mo doping were prepared as the schematic shown in Figure 1(a). A pL robotic tip dispensed a different number of precursor solution drops on preprogrammed spots on the FTO substrate to control their atomic compositions. Several identical spots of undoped $BiVO_4$ were also prepared on the top and bottom rows of the arrays to ensure the reproducibility of the dispensing system. Undoped $BiVO_4$ is also used as an internal

standard. From the second row of the array, the atomic concentration of W and Mo was controlled from 0 to 10 at %. For example, the spot at the far left top corner contains 0 at % of W and Mo, and its content of W increased up to 10 at % moving from the left to the right columns. The doping levels of Mo also increase from 0 to 10 at % from the top to the bottom rows. Both W and Mo are added to $BiVO_4$ in the middle spots of the array. The spot at the far right bottom corner has both 10 at % of W and 10 at % of Mo in $BiVO_4$, i.e., $Bi_{0.4}V_{0.4}W_{0.1}Mo_{0.1}O_x$. Note that compositions are represented in terms of the amount of reactant used in the array preparation; analysis of the spots showed actual compositions were close to these.[9]

The arrays were first scanned, observing the photocurrent from sulfite oxidation on the photocatalyst spots as shown in Figure 1(b). Those shown in Figure 1(b) yield the photocurrent measured at 0.4 V (vs NHE). The average photocurrent from the spots of undoped $BiVO_4$ in Figure 1(b) was 0.7 ± 0.2 μA. However, the photocurrent from $BiVO_4$ doped with W from 4 to 8 at % was much higher (about 7 to 9 times) than that from undoped $BiVO_4$, confirming our earlier work.[9] The photooxidation currents from $BiVO_4$ doped with 4, 6, and 8 at % of W in the array were similar to each other with a current of 6.2 ± 0.1 μA.

Doping with Mo also improved the photocurrent; e.g., $BiVO_4$ doped with 4 at % Mo showed an oxidation current of 2.6 μA, three times higher than that of undoped $BiVO_4$. The improvement of photocurrent by W doping on $BiVO_4$ was larger than that from the Mo-doped $BiVO_4$. However, photocatalyst spots, which were doped with both W and Mo, showed even greater photoactivity than $BiVO_4$ doped with W alone. Among the doubly doped photoelectrocatalysts, $BiVO_4$ doped with 2 at % W and 6 at % Mo (this particular composition is denoted as W/Mo-doped $BiVO_4$) shows the highest photooxidation current among the prepared spots. The obtained photocurrent of W/Mo-doped $BiVO_4$ in this array was 7.7 μA, which is about 25% higher than the photocurrent from W-doped $BiVO_4$.

In addition, the normalized photocurrent of those dispensed spots compared with undoped $BiVO_4$ as an internal standard was considered from several identically prepared samples with the same array configuration as that in Figure 1(a). While the photocurrent from the dispensed arrays can be affected by small changes of the incident Xe lamp beam intensity delivered through the fiber optic and by thickness variation of the dispensed spots, the relative photocurrents were quite reproducible. Thus, for five reproduced samples, the relative photocurrents normalized with respect to undoped $BiVO_4$ were 6 (±2) for 6 at % W-doped $BiVO_4$ and 9 (±3) for W/Mo-doped $BiVO_4$ (Table 1). The photocurrent of 4 at % Mo-doped $BiVO_4$ was 3.5 (±0.7), which was also higher than the photocurrent from undoped $BiVO_4$. However, the enhanced photoelectrochemical activity of W/Mo-doped $BiVO_4$ did not increase with higher doping levels of W and Mo. In fact, the photocurrent from more heavily doped samples than W/Mo-doped $BiVO_4$ with either W or Mo shows a decreased photoactivity in SECM experiments compared with the optimally doped sample.

The photoelectrochemical behavior of W/Mo-doped $BiVO_4$ was further studied in 0.1 M Na_2SO_4 solution by SECM experiments to examine oxygen evolution (Figure 2). The pL-dispensing robotic tip was also used to prepare arrays as shown in the schematic in Figure 2(a). Spot arrays of W (2 at %)-doped $BiVO_4$ with different levels of Mo doping were prepared from premixed W (2 at %)—Bi—V solution (0.1 or 0.02 M) and 0.02 M precursor solution of Mo. The current shown in Figure 2(b)

17872

dx.doi.org/10.1021/jp204492r |*J. Phys. Chem. C* 2011, 115, 17870–17879

Table 1. Summary of the Photocurrent Obtained from SECM Experiments[a]

	BiVO$_4$	Bi/V/Mo (4%)	Bi/V/W (6%)	Bi/V/W (2%)/Mo (6%)
SECM spot photocurrent (μA)	0.7 ($\pm$0.3)	2.1 ($\pm$0.3)	4 ($\pm$1)	6 ($\pm$1)
normalized current to BiVO$_4$	1	3.5 ($\pm$0.7)	6 ($\pm$2)	9 ($\pm$3)

[a] BiVO$_4$ with various different doping levels of W and Mo was prepared as shown in Figure 1. The photooxidation current of the dispensed spots was measured using SECM. Scanning of dispensed spots was performed in 0.1 M Na$_2$SO$_3$ and 0.1 M Na$_2$SO$_4$ solution at 0.4 V vs NHE under UV-visible irradiation.
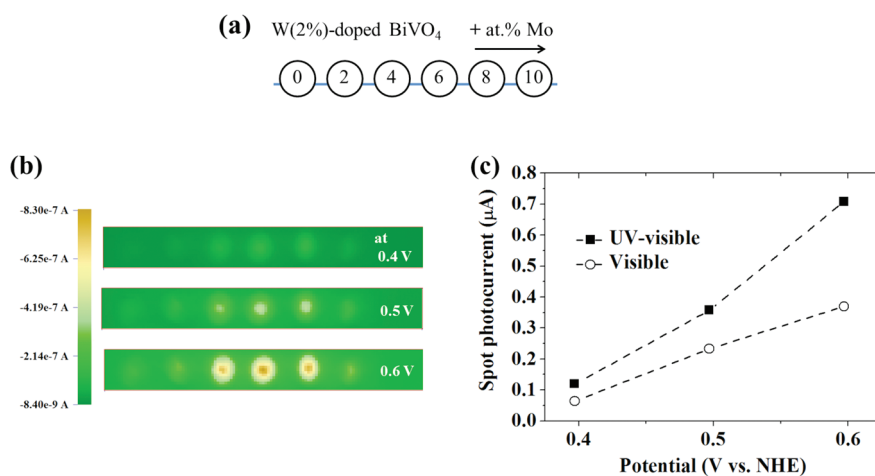
Figure 2. (a) Schematic diagram of the atomic composition of dispensed photoelectrocatalysts on FTO. Each spot has total of 18 drops of the premixed precursor solutions of W(2 at %)−Bi/V (0.1 or 0.02 M) and Mo (0.02 M) in ethylene glycol. (b) SECM images of spot arrays with different doping levels of Mo on W(2 at %)−BiVO$_4$ as shown in (a). The photocurrent for water oxidation was measured at 0.4, 0.5, and 0.6 V vs NHE in 0.1 M Na$_2$SO$_4$ solution under UV−visible irradiation. Scan rate of fiber optic was 500 μm s^{-1} (or 50 μm per 0.1 s as the setting condition of SECM), and the distance between the fiber optic and substrate was 150 μm. (c) Summary of SECM scanning of W/Mo-doped BiVO$_4$ shown in (b) under UV−visible and visible irradiation.
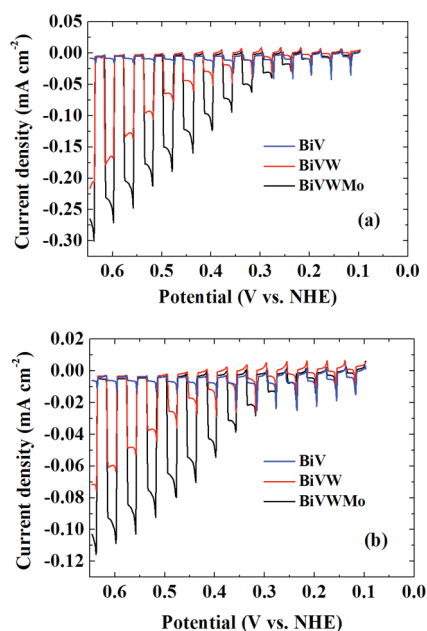
Figure 3. Linear sweep voltammograms of undoped BiVO$_4$ (blue), W-doped BiVO$_4$ (red), and W/Mo-doped BiVO$_4$ (black) with chopped light under (a) UV−visible irradiation and (b) visible irradiation in the 0.1 M Na$_2$SO$_4$ aqueous solution (pH 7, 0.2 M sodium phosphate buffered). Beam intensity was about 120 mW cm^{-2} from a full xenon lamp, and the scan rate was 20 mV s^{-1}.

measured the photocurrent for water oxidation at three different potentials, 0.2, 0.3, and 0.4 V, under UV−visible irradiation. SECM scanning at different potentials can be used to estimate the linear sweep voltammogram of bulk film electrodes from the array spot response. The results shown in Figure 2(c) for spot scanning of W/Mo-doped BiVO$_4$ for water oxidation at different potentials agree with the film voltammograms in Figure 3 when the area is normalized (correction factor of about 400). The W/Mo-doped BiVO$_4$ still shows higher photoactivity than W(2 at %)−BiVO$_4$ for water oxidation.

In addition to Mo, a number of other metal components (M) were doped into BiVO$_4$ and the spot arrays examined by SECM with the same array configuration as that in Figure 1(a) (M instead of Mo in Figure 1(a)). The results of SECM scanning of BiV−W−M, summarized in Table 2, show that doping of Tl and Zn into BiVO$_4$ increases the photocurrent for sulfite oxidation on BiVO$_4$. For example, the photoactivity of BiVO$_4$ improved about two times by doping of Tl. However, no element among the examined metal components, except Mo, showed a positive doping effect on the photoactivity of BiV−W−O.

Photoelectrochemistry with Larger Thin Bulk Film Samples. To confirm the improved photoactivity of W/Mo-doped BiVO$_4$ compared with W-doped BiVO$_4$ or undoped BiVO$_4$, thin film electrodes on FTO substrate of a larger area (2.25 cm^2) were prepared. For W-doped BiVO$_4$, the atomic ratio in between Bi, V, and W was 4.5:5:0.5, as in our previous report,[9] to achieve the maximum photocurrent in the bulk film. For W/Mo-doped BiVO$_4$, the atomic ratio between Bi, V, W, and

17873

dx.doi.org/10.1021/jp204492r |J. Phys. Chem. C 2011, 115, 17870−17879

Table 2. Summary of SECM Scanning Experiments of BiV—W—M^a

effect on BiV—O	effect on BiV—W—O	element	precursor used for spot array preparation
positive	positive	Mo	$(NH_4)_6Mo_7O_{24}$
positive	negative	Tl, Zn	$TlNO_3$, $Zn(NO_3)_2$
negative	negative	K, Cr, Fe, Co, Sr, Ir, Pb, Eu, Ga, B	KNO_3, $Cr(NO_3)_3$, $Fe(NO_3)_2$, $Co(NO_3)_2$, $Sr(NO_3)_2$, K_3IrCl_6, $Pb(NO_3)_2$, $Eu(NO_3)_3$, $Ga(NO_3)_3$, H_3BO_3

^{a} Several metal components with W were doped to $BiVO_4$ with the same array configurations as shown for Mo in Figure 1(a). Positive or negative effects of doping on the photoactivity of $BiVO_4$ and BiV—W—O were determined based on the photocurrent obtained from the scanning of dispensed spots. Scanning was performed in 0.1 M Na_2SO_3 and 0.1 M Na_2SO_4 solution at 0.4 V vs NHE under UV-visible irradiation.
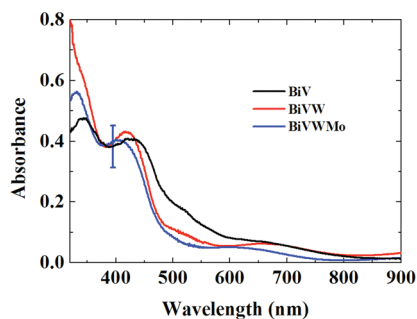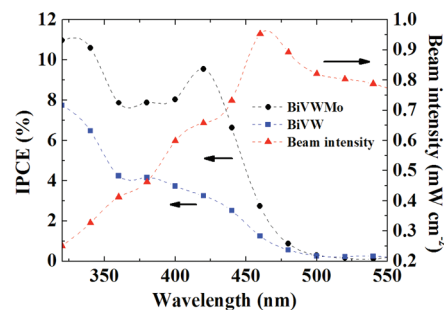

Figure 4. UV−visible absorption spectra obtained from undoped $BiVO_4$ (black), W-doped $BiVO_4$ (red), and W/Mo doped $BiVO_4$ (blue). The error bar noted at the wavelength of 400 nm for W/Mo-doped $BiVO_4$ was obtained from three different regions of the same sample to show the deviation of absorptivity by the nonuniformity of film thickness. The thickness of bulk films was around 200 nm for both electrode films.

Figure 5. IPCE plots of W-doped $BiVO_4$ (blue) and W/Mo-doped $BiVO_4$ (black) film electrodes with a thickness of about 200 nm. The photocurrent measured at 0.6 V in 0.1 M Na_2SO_4 aqueous solution. The irradiation power at the corresponding illumination at the discrete wavelength used is indicated on the plot (red). The dashed lines are added for clarity.

Mo was 4.6:4.6:0.2:0.6 according to the results from SECM experiments described above. The atomic composition of W/Mo-doped $BiVO_4$ thin film was confirmed by XPS measurement (Figure S1 and Table S1 in the Supporting Information). In addition, the surface of the prepared W/Mo-doped $BiVO_4$ was observed by scanning electron microscopy (SEM, Figure S2 in the Supporting Information). The crystal size in SEM images was usually less than 1 μm, and the surface of the film was smooth with a few holes that expose the FTO substrate through the $BiVO_4$ film.

The photocurrent shown in Figure 3 was measured in 0.1 M Na_2SO_4 solution (pH 7, 0.2 M sodium phosphates buffered) for water oxidation on the bulk film electrodes. The dramatically increased photocurrent of W-doped $BiVO_4$ with respect to undoped $BiVO_4$ is shown in Figure 3, which also agrees with our previous report.[9] The photocurrent of $BiVO_4$ for water oxidation increased from 0.01 to 0.17 mA cm^{-2} at 0.6 V by W doping under UV−visible irradiation. However, the photocurrent further improved with the consecutive doping of Mo on W-doped $BiVO_4$. The obtained photocurrent for water oxidation of W/Mo-doped $BiVO_4$ is 0.23 mA cm^{-2} at 0.6 V, which is about 40% higher than that of W-doped $BiVO_4$ under UV−visible irradiation (Figure 3(a)). The improvement of W/Mo-doped $BiVO_4$ compared with W-doped $BiVO_4$ is also observed under visible irradiation in Figure 3(b). In summary, the results using thin film electrodes confirm the results of the SECM experiments using the dispensed arrays.

Fill factors of the obtained current−potential curves in Figure 3 were found to compare the current−potential characteristic of W/Mo-doped $BiVO_4$ with that of W-doped $BiVO_4$.

To calculate the fill factor, the power density measured from the bulk film, $P_{measured}$ in mW cm^{-2} at an electrode potential of E in V, and the optimum power density, $P_{optimum}$, in mW cm^{-2}, that is the theoretical maximum power density of the ideal electrode, were defined by the following equations

$$P_{measured} = (E - E_{open\ circuit})i_{photo} \qquad (1)$$

$$P_{optimum} = (E_{short\ circuit} - E_{open\ circuit})i_{short\ circuit} \qquad (2)$$

where $E_{open\ circuit}$ is the electrode potential where the photo-oxidation current starts to flow; i_{photo} in mA cm^{-2} is an anodic photocurrent at the electrode potential of E; $E_{short\ circuit}$ is the largest electrode potential which was applied in the experiment; and $i_{short\ circuit}$ in mA cm^{-2} is the photocurrent at $E_{short\ circuit}$. Then, the fill factor is calculated as

$$\text{fill factor} = P_{max}/P_{optimum} \qquad (3)$$

where P_{max} is the maximum power density observed from the calculated $P_{measured}$. Then, the obtained fill factors are 0.17 for W/Mo-doped $BiVO_4$ and 0.12 for W-doped BiO_4 in Figure 3(a). In summary, the improved photoactivity of $BiVO_4$ by doping with W and Mo is shown as a better characteristic of the current−potential behavior. This indicates the facilitated photo-electrochemical reaction of the hole in the valence band with the species on the metal oxide electrode surface at the low over-potential region.

UV−visible absorption spectra of the thin film electrodes are shown in Figure 4. The thickness of the thin films used for the absorption measurements, measured by SEM from the cross-section images of the films on FTO substrate, was about 200 nm. The error bar shown in the absorption spectrum of
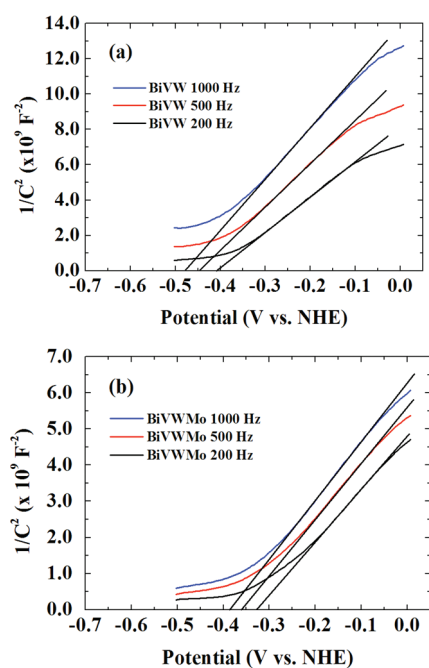
Figure 6. Mott−Schottky plots of (a) W-doped BiVO₄ and (b) W/Mo-doped BiVO₄ obtained from the capacitance measurements. AC amplitude of 10 mV was applied for each potential, and three different AC frequencies were used for the measurements: 1000 Hz (blue), 500 Hz (red), and 200 Hz (black). Tangent lines of the M−S plots are drawn to obtain the flat band potential.

W/Mo-doped BiVO₄ at a wavelength of 400 nm is the deviation of absorbance caused by thickness variations within the film prepared by drop casting on an FTO substrate. Within this variation, the absorption spectra of W-doped BiVO₄ and W/Mo-doped BiVO₄ do not show significant differences. In addition, the ratio of the photocurrent under visible irradiation (>420 nm) to that under UV−visible irradiation is similar for both W/Mo-doped BiVO₄ and W-doped BiO₄, ∼0.4 (Figure 3). We thus conclude that the enhanced photoactivity of W/Mo-doped BiVO₄ compared with W-doped BiVO₄ does not originate from any difference in the light absorbance or optical properties, i.e., E_g.

IPCE measurements of W/Mo-doped BiVO₄ and W-doped BiVO₄ were also performed as shown in Figure 5. The photocurrents measured at 0.6 V under monochromatic irradiation were used to calculate the ratio of photogenerated power to the incidence irradiation power according to the following equation

$$\text{IPCE } (\%) = (1240/\lambda) \times i_{\text{ph}}/P_{\text{in}} \times 100 \tag{4}$$

where λ is the wavelength of illuminated light in nm; i_{ph} is the measured photocurrent density in mA cm⁻²; and P_{in} is the incident power density in mW cm⁻². To obtain the photooxidation current, linear sweep voltammetry (LSV) was performed with and without the light irradiation for each monochromatic wavelength, and the current difference between two voltammograms at 0.6 V was taken as the photocurrent. The reported IPCE depends upon the nature of the reaction (i.e., water oxidation vs sacrificial donor oxidation), the applied potential, the wavelength of the irradiation, and the thickness and absorbance of the photocatalyst film. In Figure 5 the potential used for the IPCE measurements is less than the thermodynamic potential for water oxidation, ∼0.8 V, under the experimental conditions. The scan

rate was 20 mV s⁻¹, and the potential was swept from 0.1 to 0.65 V. In the IPCE spectrum, the photooxidation current starts to flow from about 500 nm, which indicates that both W/Mo-doped BiVO₄ and W-doped BiVO₄ have a band gap size of 2.4−2.5 eV, which is similar to that of undoped BiVO₄. So, the enhanced photoactivity of W/Mo-doped BiVO₄ compared with W-doped BiVO₄ or undoped BiVO₄ is not raised from the modification of band gap size. However, IPCE measurements still show the improved photoactivity of W/Mo-doped BiVO₄ over W-doped BiVO₄ under a low intensity monochromatic irradiation. In consideration of the similar absorbance and band gap size, the enhanced water photooxidation of the W/Mo-doped BiVO₄ electrode over the W-doped BiVO₄ electrode is not from modified absorption properties by the consecutive doping of W and Mo in BiVO₄ but rather from a better separation of the excited hole and electron pair.

Mott−Schottky Plots. Capacitance measurements were conducted to obtain a Mott−Schottky plot (Figure 6). The flat band potential of semiconductor film in a liquid junction can be estimated from the Mott−Schottky equation[29]

$$1/C_{\text{sc}}^{2} = (2/e\varepsilon\varepsilon_0 N_{\text{D}})(E - E_{\text{fb}} - kT/e) \tag{5}$$

where C_{sc} is the space charge capacitance in F cm⁻²; e is the electronic charge in C; ε is the dielectric constant of the semiconductor; ε_0 is the permittivity of free space; N_{D} is the carrier density in cm⁻³; E is the applied potential in V; E_{fb} is the flat band potential in V; κ is the Boltzmann constant; and T represents the temperature in K. The temperature related term ($\kappa T/e$) in eq 5 is negligible, 0.0257, at room temperature. The flat band potential is obtained from the x-intercept of the tangent line of the Mott−Schottky (M−S) plot on potential axis. The flat band potential of W/Mo-doped BiVO₄ in 0.1 M Na₂SO₄ solution, from the results at a frequency of 1000 Hz, is about −0.4 V, which is about 0.1 V positive compared to that of W-doped BiVO₄.

However, the flat band potential obtained from the Mott−Schottky plot shows a frequency dependency as shown in Figure 6. The nonconverging frequency dependency of the Mott−Schottky plot might originate from nonideality of the surface of a drop cast semiconductor film on FTO for the capacitance measurement,[30] e.g., from the many grain boundaries of polycrystalline BiVO₄ and an inhomogeneous distribution of crystal sizes over the film surface. Although the carrier density (N_{D}) of the semiconductor can, in principle, also be calculated from the slope of the Mott−Schottky plot, the quantitative analysis on the carrier density of the films was not performed because of the nonideal behavior of the Mott−Schottky plot as described above because of nonideality of the films, including different roughness factors between the samples and the effects of exposed FTO. However, the carrier density of W/Mo-doped BiVO₄ is about twice that of W-doped BiVO₄ as shown in the slope of the Mott−Schottky plots. In summary, W/Mo-doped BiVO₄ shows a positive shift of the flat band position of about 0.1 V compared with W-doped BiVO₄ and shows higher donor density than W-doped BiVO₄.

The photocatalytic activity of BiVO₄ is significantly affected by the crystal structure. For example, BiVO₄, with a monoclinic scheelite-like structure, shows several hundred times higher photocatalytic activity in aqueous AgNO₃ solution than the tetragonal scheelite structure BiVO₄.[15] The band gap of tetragonal BiVO₄ is bigger than monoclinic BiVO₄, 2.9 vs 2.5 eV, for
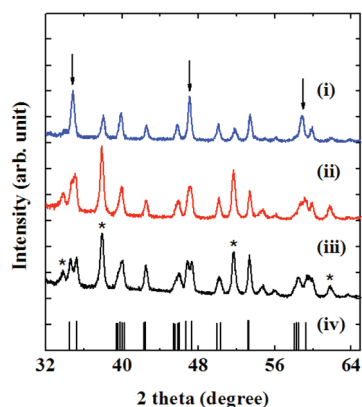
Figure 7. XRD patterns of (i) 2 at % W and 6 at % Mo-doped BiVO$_4$, (ii) 5 at % W-doped BiVO$_4$, and (iii) undoped BiVO$_4$. The reference patterns of the monoclinic scheelite-like BiVO$_4$ (iv, PDF #14-0688) and patterns from the FTO substrate (*) are also indicated. Arrows indicate the shift of peaks as its atomic composition varied from pristine BiVO$_4$ to BiVO$_4$ doped by W and Mo.
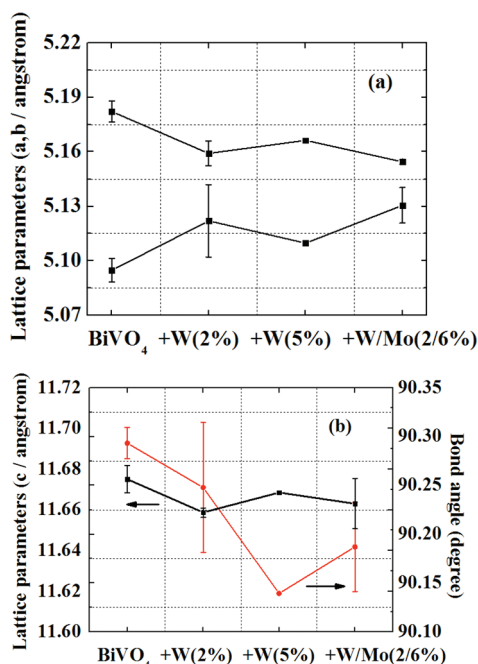
Figure 8. Lattice parameters estimated from Rietveld refinement of the XRD patterns which are shown in Figure 7. The refinement was performed by the MAUD program for undoped BiVO$_4$, 2 at % W-doped BiVO$_4$, 5 at % W-doped BiVO$_4$, and 2 at % W and 6 at % Mo-doped BiVO$_4$.

the tetragonal and monoclinic BiVO$_4$, respectively, but the reason for the significant differences in photoactivity for the different crystal structures has not been clearly elucidated. The structure of BiVO$_4$ is also deformed by adding W and Mo; this was studied using XRD analysis (Figure 7 and Figure 8). W-doped BiVO$_4$ and W/Mo-doped BiVO$_4$ show major peaks of the monoclinic scheelite-like BiVO$_4$ (PDF #14-0688) in Figure 7 and in a wider range of diffractograms in Figure S3 in the Supporting Information. No noticeable peaks appeared from any secondary phases in the XRD patterns. Thus, the result from XRD measurements indicates that W and Mo can be dissolved at
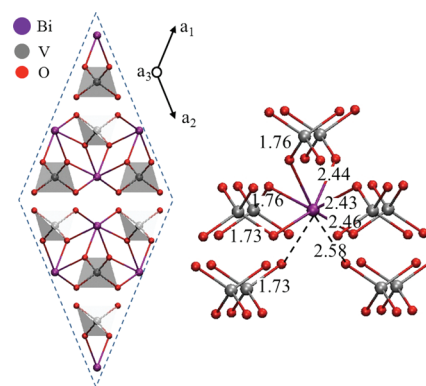
Figure 9. Base-centered monoclinic structure of BiVO$_4$ with primitive unit cell vectors (a$_1$, a$_2$, and a$_3$). Purple, silver, and red balls represent Bi, V, and O atoms, respectively. The bond lengths indicated are given in Å.

up to 8 at % as a solid solution in BiVO$_4$ without the formation of other secondary phases such as WO$_x$ or MoO$_x$.

However, there is an observable shift of the XRD patterns by adding W and Mo to the monoclinic BiVO$_4$. The shift and merging of peaks are indicated by arrows at 34°, 47°, and 59° in Figure 7. The peaks at 34.5° and 35.2° are indexed to the (2 0 0) and (0 0 2) lattices of the monoclinic scheelite-like BiVO$_4$ (Figure 7(iii)). By adding 5 at % W to BiVO$_4$, the two peaks closely shift toward each other, and the two peaks finally merge into a single peak when 2 at % W and 6 at % Mo are doped into BiVO$_4$. Similar behavior is also observed for the peaks at 46.7° and 47.9° which are indexed to the (2 4 0) and (0 4 2) lattices of the monoclinic scheelite-like BiVO$_4$. They first shift toward each other at low doping levels of W (Figure 7(ii)), and then the peaks merge into a single peak with higher doping levels of W and Mo (Figure 7(i)). A small peak also appeared at 59.4° which is closely placed to the peak at 59.9° for undoped BiVO$_4$. The peak at 59.4° shifts toward and finally merges with the peak at 58.4° during consecutive doping of W and Mo into BiVO$_4$.

The Rietveld refinement of the XRD patterns reveals the deformation of the crystal structure of monoclinic scheelite-like BiVO$_4$ with doping of W and Mo (Figure 8). The results indicate that the cell dimensions and the crystal symmetry of BiVO$_4$ continuously change from monoclinic to tetragonal with doping of W and Mo. The structural deformation and the changes of crystal symmetry of BiVO$_4$ obtained in this study agree well with the results from Sleight et al. reported in 1975.[14] Sleight also suggested the formation of catalytically active defect vacancies on the crystal surface by doping of W or Mo into BiVO$_4$, but the analysis obtained here cannot determine the existence of vacancies on the surface of BiVO$_4$. The crystal deformation might be caused by a substitutional defect of V^{5+} ions being replaced by W^{6+} and Mo^{6+}, both of which have larger tetrahedral ionic radii than V^{5+} (tetrahedral ionic radii for V^{5+}, Mo^{6+}, and W^{6+} are 0.35, 0.41, and 0.42 Å, respectively).[31] However, the relationship of the crystal deformation of BiVO$_4$ with the corresponding photoelectrochemical properties has not been clearly explained, and further investigation is needed.

■ THEORETICAL CALCULATIONS

DFT calculations were performed to understand better the effects of doping on the electronic structure and the subsequent photocatalytic performance of BiVO$_4$. For reference sake, we first
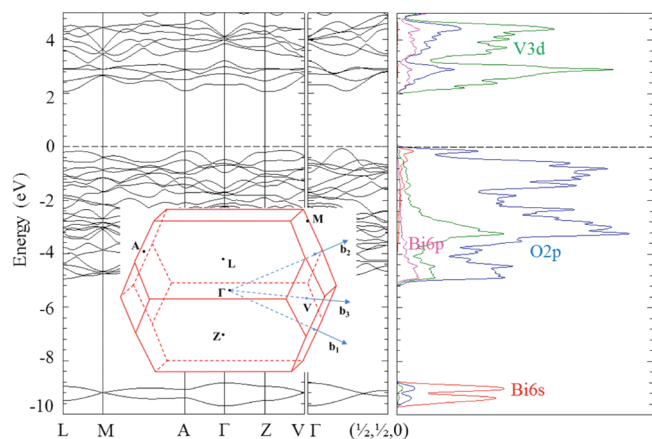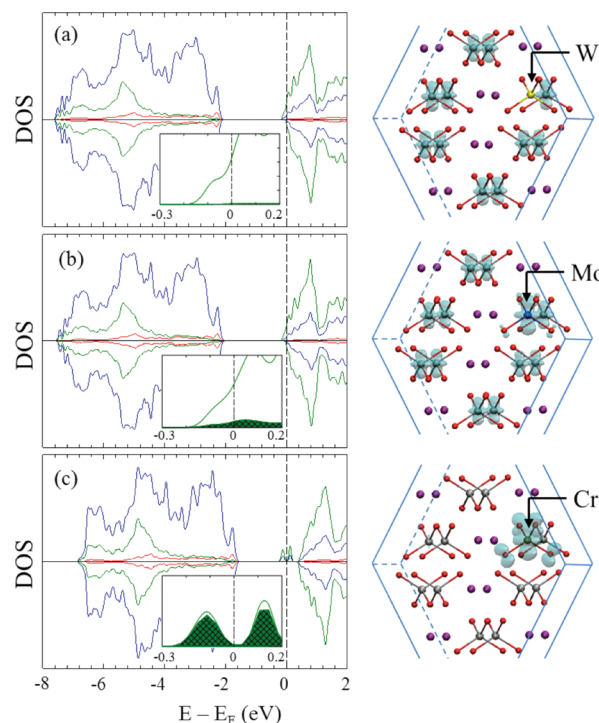
Figure 10. Electronic band structure and density of states projected onto the Bi 6s (red), Bi 6p (pink), O 2p (blue), and V 3d (green) states. The horizontal dotted line indicates the Fermi energy level, which is set to 0 eV. In the inset, the Brillouin zone for monoclinic $BiVO_4$ is shown with reciprocal lattice vectors (b_1, b_2, and b_3) and selected high-symmetry k-points (Γ, L, M, A, Z), as indicated.
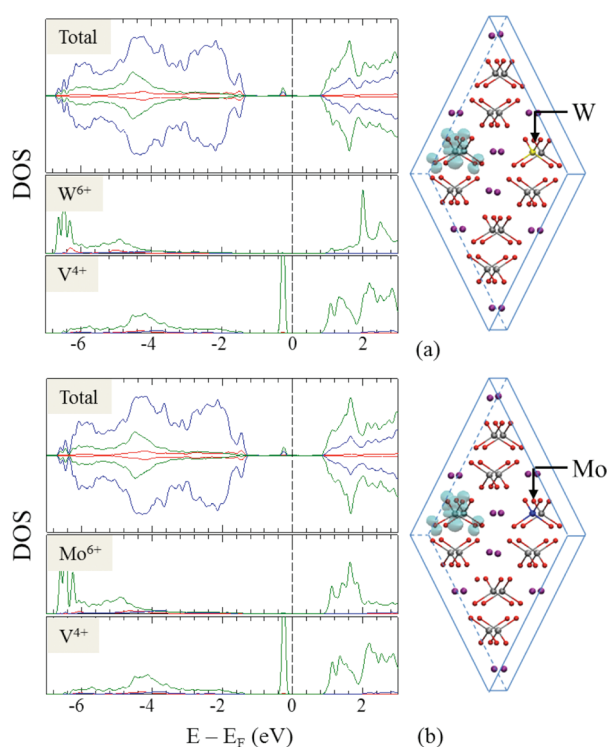

Figure 11. Total density of states (DOS) (left panels) and isosurfaces (0.02 electron/$Å^3$) of band-decomposed excess electron densities (right panels) of (a) W-, (b) Mo-, and (c) Cr-doped $BiVO_4$, from DFT (GGA) calculations. In the DOS plots, the red, blue, and green solid lines indicate the s, p, and d states, respectively, and the shaded areas (in the insets) correspond to the contributions from the W 5d, Mo 4d, and Cr 3d states, as indicated. In the right panels, purple, silver, and red balls represent Bi, V, and O atoms, respectively; the positions of W (in yellow), Mo (blue), and Cr (brown) are also indicated. All Bi−O bonds are omitted for clarity.

determined the atomic and electronic structures of monoclinic scheelite-like $BiVO_4$ (space group $C2/c$ (#15)).[27] As illustrated in Figure 9, the $BiVO_4$ structure exhibits a distorted Bi−O dodecahedron with four unequal pairs of Bi−O bond distances (2.43, 2.44, 2.46, and 2.58 Å), attributed to the Bi^{3+} off-centering;[32,33] accordingly, it also shows a slightly distorted VO_4^{3-} tetrahedron with two pairs of V−O bond distances (1.73 and 1.76 Å).

Figure 10 shows the density of states (DOS) projected onto the atomic orbitals for Bi, V, and O ions, together with corresponding band structures along high symmetry directions in the Brillouin zone. The Bi−O interaction leads to the hybridization between the Bi 6s and O 2p states into the bonding state (in the range 9−10 eV below the Fermi level) and the antibonding state (near the valence band maximum); subsequently, the filled antibonding state is stabilized by mixing with the empty Bi 6p states, leaving a stereochemically active $6s^2$ lone pair on the Bi^{3+} ion.[17,33]

As shown in Figure 10, the band structure of $BiVO_4$ has a direct gap located midway between Γ and (1/2, 1/2, 0) (as indicated), according to our DFT-GGA calculations, which appears to be slightly smaller than the previously reported gap at A.[17] The valence band maximum (VBM) and conduction band minimum (CBM) are likely composed of the Bi 6s/Bi 6p/O 2p and V 3d/O 2p/Bi 6p hybridized states, respectively. The predicted gap of 2.15 eV is smaller than the experimental value of 2.4−2.5 eV, while it is well-known that DFT typically underestimates the band gap in insulators and semiconductors.[34] From the curvatures of the band edges, the effective hole and electron masses are roughly estimated to be $0.42m_e$ and $0.60m_e$, respectively. Overall, our calculations are consistent with previous calculations and experiments.[13,17,27,32,33]

Doping-induced changes in the host $BiVO_4$ structure were examined by replacing one of the 16 V atoms in the supercell (i.e., a larger cell that contains several $BiVO_4$ primitive cells) employed with W, Mo, and Cr atoms (corresponding to a doping concentration of 6.25%). Like the VO_4 case, the CrO_4, MoO_4, and WO_4 tetrahedra are also slightly distorted with two unequal bond lengths of 1.71/1.73 Å, 1.80/1.81 Å, and 1.80/1.81 Å,

respectively. These impurity atoms have one more valence electron than the V host atom; hence their substitution into the host lattice provides an extra electron per impurity.

In metal oxides, excess charge carriers, electrons and holes, may form small and/or large polarons (e.g., an electron with associated polarization field extending of short or long distance); the former localize at the atomic scale, and the latter are extended over several lattice sites.[35] The microscopic description of charge localization strongly depends on the method employed. The conventional DFT-GGA approach has an intrinsic tendency to erroneously favor delocalization of charge carriers. The strongly correlated nature of the d-electrons in metal oxides can be better described by adding a Hubbard-U term to the DFT energy functional; however, in the DFT + U scheme, the result is a strong function of the interaction parameter, U; i.e., the degree of charge localization increases with U. While no experimental evidence is available in the literature for the formation of localized charge carriers in bulk $BiVO_4$, we performed electronic structure analysis of the doped $BiVO_4$ with W, Mo, and Cr at both $U = 0$ and sufficiently large U values for the d orbitals of V, Mo, and W.

At $U = 0$, the electron DOS profiles for the doped $BiVO_4$ supercells with W [(a)], Mo [(b)], and Cr [(c)] are shown in Figure 11. In the W- and Mo-doped cases, the Fermi level is located inside the conduction band, indicating partial filling of the V 3d states; that is, the excess electron is delocalized over the

Figure 12. Total and projected density of states (DOS) (left panels) and isosurfaces (0.02 electron/Å^3) of band-decomposed excess electron densities (right panels) of (a) W- and (b) Mo-doped BiVO$_4$, from DFT(GGA)+U calculations. In the DOS plots, the red, blue, and green solid lines indicate the s, p, and d states, respectively. In the right panels, purple, silver, and red balls represent Bi, V, and O atoms, respectively; the positions of W (in yellow) and Mo (in blue) are also indicated. All Bi−O bonds are omitted for clarity.

V ions while filling the conduction band minimum. On the other hand, the excess electron tends to localize on the Cr ion in Cr-BiVO$_4$; the localized Cr^{5+} impurity state appears in the gap. The difference can be understood by comparing the d-orbital energy levels of Cr, Mo, W, and V (Cr 3d < Mo 4d ≈ W 3d < W 5d).[36,37] These results demonstrate that the Cr^{5+} substitutional ions will serve as both charge traps and recombination centers,[38] thereby degrading the photocatalytic performance of BiVO$_4$, which is consistent with our experiments (Figure S4 in the Supporting Information). We also find that there is no noticeable change in the shape of the valence and conduction band edges, while the gap slightly (<0.1 eV) increases with W- and Mo-doping. This may suggest that hole and electron effective masses, and subsequently their mobilities, would be weakly affected by the doping, if carrier transport is mainly governed by the band conduction of large polarons.

Provided that W and Mo are shallow donors, we further attempted to examine the difference in the photocatalytic performance of W- and Mo-doped BiVO$_4$ by calculating W and Mo ionization energies ($\varepsilon_{M}^{(0/+)}$, M = Mo and W). The ionization energy can be given by[39]

$$\varepsilon_{M}^{(0/+)} = E_{tot,M}^{(0)} - E_{tot,M}^{(+)} - \varepsilon_{VBM}$$

where $E_{tot,M}^{(0)}$ and $E_{tot,M}^{(+)}$ are the total energies of the doped supercells in the neutral and positive charge states, respectively, and ε_{VBM} is the position of the valence band maximum. Hence, the ionization level difference between W and Mo is estimated to

be 0.02 eV [= $\varepsilon_{W}^{(0/+)} - \varepsilon_{Mo}^{(0/+)} = (E_{tot,W}^{(0)} - E_{tot,W}^{(+)}) - (E_{tot,Mo}^{(0)} - E_{tot,Mo}^{(+)})$], demonstrating that W can more efficiently donate electrons to the host lattice than Mo. The increased carrier density may lead to enhanced photocatalytic performance by possibly increasing the electric field in the space-charge layer, as the increased electric field may lead to enhancement in the separation of photogenerated electrons and holes, as suggested by earlier experiment.[40]

Next, we applied the DFT + U approach with U = 2.7 eV[41] for the V 3d states in BiVO$_4$; as shown in Figure 12, the band gap of BiVO$_4$ increases to 2.29 eV, while the shape of the electronic band structure remains nearly unchanged. The chosen U value is sufficiently large such that excess electrons localize spatially at the V sites; in the literature the commonly applied U values for V 3d are in the range of 2−4 eV.[41−43] For the W- and Mo-doped cases, U = 2.3 eV for Mo 4d and U = 2.1 eV for W 5d were chosen, according to ref 41. Note that 4d- and 5d-valence orbitals are generally less spatially localized than 3d-valence orbitals, such that corresponding U values are accordingly smaller. The properties of doped BiVO$_4$ can be affected by the choice of U, but these DFT+U calculations should be appropriate to draw reasonable conclusions regarding the localization of excess electrons.

According to the DFT+U calculations, the excess electron from W or Mo favorably localizes on a V atom and creates a localized state in the band gap, as demonstrated by analysis of the electronic DOS and the (band decomposed) excess electron density (Figure 12). The small polaron formation involves a sizable lattice distortion around the reduced V^{4+} ion. The excess electron residing at the V^{4+} site may undergo migration to an adjacent V^{5+} (or Mo^{6+}, W^{6+}) site; the small polaron transport usually follows a thermally activated hopping mechanism. As reasoned earlier, the electron donation from W to the host lattice would be more favorable than from Mo. This may result in enhanced charge carrier mobility because a higher concentration of small polarons would lead to a larger overlap between them, thereby lowering the activation energy for polaron hopping.[44−46] On the basis of the results, we speculate that an increase in the charge carrier concentration for the host lattice would lead to enhanced photocatalytic performance, unless the concentration of dopants is so high that they, as scattering centers, significantly impede charge transport. This is consistent with earlier experimental observations suggesting that the increase in carrier concentration would be often responsible for the enhanced activity of doped photocatalysts[47] and may also provide an explanation for the better photocatalytic performance of W−BiVO$_4$ over Mo−BiVO$_4$, as reported in this paper.

■ CONCLUSION

SECM has been used to screen the fifth material as the dopant for the n-type W-doped BiVO$_4$ to improve the photoactivity for water oxidation. Consecutive doping of W and Mo into the BiVO$_4$ dramatically increases the photooxidation current of water on the BiVO$_4$ electrode. The W/Mo-doped BiVO$_4$ shows more than 10 times higher photocurrent for water oxidation than undoped BiVO$_4$. Also, the rapid screening method by SECM has been shown to be a tool to develop an active photocatalyst such as W/Mo-doped BiVO$_4$. Capacitance measurements reveal a shift in the flat band position of W/Mo-doped BiVO$_4$ by Mo doping into W-doped BiVO$_4$. XRD analysis confirms a solid solution of W/Mo-doped BiVO$_4$ without the formation of secondary phases. Furthermore, deformation of crystal structure

of the scheelite $BiVO_4$ occurs with consecutive doping of W and Mo with the crystal symmetry shifting from monoclinic to tetragonal. W and Mo are revealed as the excellent shallow dopants, which facilitate the separation of excited electron−hole pairs in the photocatalyst. However, further study in a better defined sample, e.g., single-crystal $BiVO_4$, is desirable in elucidating the role of dopants in $BiVO_4$ PEC.

■ ASSOCIATED CONTENT

Ⓢ Supporting Information. XRD, XPS, SEM, and additional SECM data. This material is available free of charge via the Internet at http://pubs.acs.org.

■ AUTHOR INFORMATION

Corresponding Author
*E-mail: ajbard@mail.utexas.edu.

■ ACKNOWLEDGMENT

■ REFERENCES

(1) Bard, A. J.; Fox, M. A. *Acc. Chem. Res.* **1995**, *28*, 141–145.

(2) Bard, A. J. *J. Phys. Chem.* **1982**, *86*, 172–177.

(3) Woodhouse, M.; Parkinson, B. A. *Chem. Soc. Rev.* **2009**, *38*, 197–210.

(4) Baeck, S. H.; Jaramillo, T. F.; Brandli, C.; McFarland, E. W. *J. Comb. Chem.* **2002**, *4*, 563–568.

(5) Lee, J.; Ye, H.; Pan, S.; Bard, A. J. *Anal. Chem.* **2008**, *80*, 7445–7450.

(6) Jang, J. S.; Lee, J.; Ye, H.; Fan, F.-R. F.; Bard, A. J. *J. Phys. Chem. C* **2009**, *113*, 6719–6724.

(7) Jang, J. S.; Yoon, K. Y.; Xiao, X.; Fan, F.-R. F.; Bard, A. J. *Chem. Mater.* **2009**, *21*, 4803–4810.

(8) Liu, W.; Ye, H.; Bard, A. J. *J. Phys. Chem. C* **2010**, *114*, 1201–1207.

(9) Ye, H.; Lee, J.; Jang, J. S.; Bard, A. J. *J. Phys. Chem. C* **2010**, *114*, 13322–13328.

(10) Liu, G.; Liu, C.; Bard, A. J. *J. Phys. Chem. C* **2010**, *114*, 20997–21002.

(11) Fujishima, A.; Honda, K. *Nature* **1972**, *238*, 37–38.

(12) Bard, A. J. *J. Am. Chem. Soc.* **2010**, *132*, 7559–7567.

(13) Yao, W.; Ye, J. *J. Phys. Chem. B* **2006**, *110*, 11188–11195.

(14) Sleight, A. W.; Aykan, K.; Rogers, D. B. *J. Solid State Chem.* **1975**, *13*, 231–236.

(15) Tokunaga, S.; Kato, H.; Kudo, A. *Chem. Mater.* **2001**, *13*, 4624–4628.

(16) Sayama, K.; Nomura, A.; Arai, T.; Sugita, T.; Abe, R.; Yanagida, M.; Oi, T.; Iwasaki, Y.; Abe, Y.; Sugihara, H. *J. Phys. Chem. B* **2006**, *110*, 11352–11360.

(17) Walsh, A.; Yan, Y.; Huda, M. N.; Al-Jassim, M. M.; Wei, S.-H. *Chem. Mater.* **2009**, *21*, 547–551.

(18) Myung, N.; Ham, S.; Choi, S.; Chae, Y.; Kim, W.-G.; Jeon, Y. J.; Paeng, K.-J.; Chanmanee, W.; de Tacconi, N. R.; Rajeshwar, K. *J. Phys. Chem. C* **2011**, *115*, 7793–7800.

(19) Van de Krol, R.; Liang, Y.; Schoonman, J. *J. Mater. Chem.* **2008**, *18*, 2311–2320.

(20) Kudo, A.; Omori, K.; Kato, H. *J. Am. Chem. Soc.* **1999**, *121*, 11459.

(21) Sayama, K.; Nomura, A.; Arai, T.; Sugita, T.; Abe, R.; Yanagida, M.; Oi, T.; Iwasaki, Y.; Abe, Y.; Sugihara, H. *J. Phys. Chem. B* **2006**, *110*, 11352–11360.

(22) Ferrari, M.; Lutterotti, L. *J. Appl. Phys.* **1994**, *76*, 7246–7255.

(23) Perdew, J. P.; Burke, K.; Ernzerhof, M. *Phys. Rev. Lett.* **1996**, *77*, 3865–3868.

(24) Kresse, G.; Furthmuller, J. *VASP the Guide*; Vienna University of Technology: Vienna, 2001.

(25) Blöchl, P. E. *Phys. Rev. B* **1994**, *50*, 17953–17979.

(26) Monkhorst, H. J.; Pack, J. D. *Phys. Rev. B* **1976**, *13*, 5188–5192.

(27) Liu, J. C.; Chen, J. P.; Li, D. L. *Acta Phytophysiol. Sin.* **1983**, *32*, 1053–1060.

(28) Dudarev, S. L.; Botton, G. A.; Savrasov, S. Y.; Humphreys, C. J.; Sutton, A. P. *Phys. Rev. B* **1998**, *57*, 1505–1509.

(29) Bard, A. J.; Faulkner, L. R. *Electrochemical Methods Fundamentals and Application*, 2nd ed.; John Wiley & Sons: New York, 2001; pp 746−752.

(30) Cardon, F.; Gomes, W. P. *J. Phys. D: Appl. Phys.* **1978**, *11*, L63–L67.

(31) Corbel, G.; Laligant, Y.; Goutenoire, F.; Suard, E.; Lacorre, P. *Chem. Mater.* **2005**, *17*, 4678–4684.

(32) David, W. I. F.; Wood, I. G. *J. Phys. C: Solid State Phys.* **1983**, *16*, 5127–5148.

(33) Stoltzfus, M. W.; Woodward, P. M.; Seshadri, R.; Klepeis, J.-H.; Bursten, B. *Inorg. Chem.* **2007**, *46*, 3839–3850.

(34) Perdew, J. P. *Int. J. Quantum Chem.* **1985**, *28*, 497–523.

(35) Sumi, H. *J. Phys. Soc. Jpn.* **1972**, *33*, 327–342.

(36) Yin, W. -J.; Tang, H.; Wei, S.-H.; Al-Jassim, M. M.; Turner, J.; Yan, Y. *Phys. Rev. B* **2010**, *82*, 045106-1–045106-6.

(37) Osorio-Guillen, J.; Lany, S.; Zunger, A. *Phys. Rev. Lett.* **2008**, *100*, 036601-1–036601-4.

(38) Gai, Y.; Li, J.; Li, S.-S.; Xia, J.-B.; Wei, S.-H. *Phys. Rev. Lett.* **2009**, *102*, 036402-1–036402-4.

(39) Mattioli, G.; Alippi, P.; Filippone, F.; Caminiti, R.; Bonapasta, A. A. *J. Phys. Chem. C* **2010**, *114*, 21694–21704.

(40) Cesar, I.; Sivula, K.; Kay, A.; Zboril, R.; Gratzel, M. *J. Phys. Chem. C* **2009**, *113*, 772–782.

(41) Solovyev, I. V.; Dederichs, P. H. *Phys. Rev. B* **1994**, *50*, 16861–16871.

(42) Kozhevnikov, A. V.; Anisimov, V. I.; Korotin, M. A. *Phys. Met. Metall.* **2007**, *104*, 215–220.

(43) Cox, B. N.; Coulthard, M. A.; Lloyd, P. *J. Phys. F: Metal Phys.* **1974**, *4*, 807–820.

(44) Ruscher, C.; Salje, E.; Hussain, A. *J. Phys. C: Solid State Phys.* **1988**, *21*, 3737–3749.

(45) Neupane, K. P.; Cohn, J. L.; Terashita, H.; Neumeier, J. J. *Phys. Rev. B* **2006**, *74*, 144428-1–144428-5.

(46) Liu, L.; Guo, H.; Lü, H.; Dai, S.; Cheng, B.; Chen, Z. *J. Appl. Phys.* **2005**, *97*, 054102-1– 054102-5.

(47) Hu, Y.-S.; Kleiman-Shwarsctein, A.; Forman, A. J.; Hazen, D.; Park, J.-N.; McFarland, E. W. *Chem. Mater.* **2008**, *20*, 3803–3805.

17879

dx.doi.org/10.1021/jp204492r |*J. Phys. Chem. C* 2011, 115, 17870–17879